4-19-2017

Dust-polarization Maps and Interstellar Turbulence

Robert R. Caldwell
Dartmouth College

Chris Hirata
The Ohio State University

Marc Kamionkowski
Johns Hopkins University

The Astrophysical Journal, 839:91 (12pp), 2017 April 20 https://doi.org/10.3847/1538-4357/aa679c

Dust-polarization Maps and Interstellar Turbulence

Robert R. Caldwell[1], Chris Hirata[2], and Marc Kamionkowski[3]
[1] Department of Physics and Astronomy, 6127 Wilder Laboratory, Dartmouth College, Hanover, NH 03755, USA
[2] Center for Cosmology and Astroparticle Physics, The Ohio State University, 191 West Woodruff Lane, Columbus, OH 43210, USA
[3] Department of Physics and Astronomy, Johns Hopkins University, 3400 North Charles Street, Baltimore, MD 21218, USA
Received 2016 August 26; revised 2017 March 14; accepted 2017 March 15; published 2017 April 19

Abstract

Perhaps the most intriguing result of Planck's dust-polarization measurements is the observation that the power in the *E*-mode polarization is twice that in the *B* mode, as opposed to pre-Planck expectations of roughly equal dust powers in the *E* and *B* modes. Here we show how the *E*- and *B*-mode powers depend on the detailed properties of the fluctuations in the magnetized interstellar medium (ISM). These fluctuations can be decomposed into slow, fast, and Alfvén magnetohydrodynamic (MHD) waves, which comprise a complete basis that can be used to describe linear fluctuations of a magnetized fluid. They can alternatively be decomposed in terms of one longitudinal and two transverse components of a fluid-displacement field. The intensity (*T*) and *E*- and *B*-mode amplitudes induced by each of the three types of waves, in both decompositions, are then calculated. To illustrate how these tools can be applied, we consider a toy model of the ISM in which dust traces a single component of plasma, and obtain the *EE/BB* ratio and *TE* correlation for several ansatzes for the power in slow/fast/Alfvén waves and in longitudinal/transverse waves. Although our model may be too simplistic to properly describe the nonlinear structure of interstellar magnetic fields, we find that the observed *EE/BB* ratio (and its scale invariance) and positive *TE* correlation—as well as the observed power-law index for the angular spectrum of these fluctuations—are not easily accommodated in terms of simple MHD turbulence prescriptions for the expected powers in slow, fast, and Alfvén waves. We speculate that the ∼0.1–30 pc length scales probed by these dust-polarization measurements are not described by MHD turbulence, but rather probe the large-scale physics that drives ISM turbulence. We find that a slightly anisotropic spectrum of random fluid displacements produces $EE/BB \simeq 2$ and a positive *TE* cross-correlation. Furthermore, we find that large *EE/BB* and positive *TE* are due primarily to longitudinal, rather than transverse, modes in the random-displacement field, providing, perhaps, some clue to the mechanism that stirs the ISM. Future investigations involving the spatial dependence of the *EE/BB* ratio, *TE* correlation, and local departures from statistical isotropy in dust-polarization maps, as well as further tests of some of the assumptions in this analysis, are outlined. This work may also aid in the improvement of foreground-separation techniques for studies of cosmic microwave background polarization.

Key words: ISM: general – cosmic background radiation

1. Introduction

The *Planck* satellite has provided an extraordinary trove of detailed information on polarized emission from dust in the interstellar medium (ISM) of the Milky Way (Ade et al. 2015a), with precise power spectra measured over the multipole-moment range $30 \lesssim \ell \lesssim 600$ (Adam et al. 2016a). Since the polarization of the dust emission arises from the alignment of spinning dust grains with the magnetic field (Chandrasekhar & Fermi 1953; Stein 1966; Dolginov 1972; Dolginov & Mytrophanov 1976; Draine & Weingartner 1996, 1997; Finkbeiner et al. 2004; Draine & Fraisse 2009; Andersson et al. 2015), the measurements are particularly important for the magnetic field structure of the ISM.

Perhaps the most surprising result from *Planck* is the discovery that the *E*-mode power in the dust-polarization is twice the *B*-mode power (Adam et al. 2016a). (Something similar was noticed in *WMAP*, albeit with less significance, with synchrotron polarization; Page et al. 2007). The linear-polarization pattern can be decomposed geometrically into two rotational invariants, the *E* (gradient) modes and *B* (curl) modes (Kamionkowski et al. 1997b; Zaldarriaga & Seljak 1997). A randomly oriented polarization map should have equal *E*- and *B*-mode powers. Likewise, if polarization fluctuations arise as amplitude fluctuations with a fixed orientation, then the *E*- and *B*-mode powers should be equal (Zaldarriaga 2001; Kamionkowski & Kovetz 2014). The state-of-the-art pre-Planck dust-polarization models (O'Dea et al. 2012; Delabrouille et al. 2013) therefore all had equal *E*- and *B*-mode powers. The observed $EE/BB \simeq 2$ ratio thus comes as quite a surprise. *Planck* also finds a cross-correlation (of positive sign) between the temperature and the *E*-mode component of polarization, an empirical fact that we will also employ below.

Here we show how the observed $EE/BB \simeq 2$ ratio depends on the detailed properties of magnetized fluid fluctuations in the ISM. Fluctuations in a magnetized plasma are described most generally by the slow, fast, and Alfvén MHD waves; there is one for each Fourier wavevector $\boldsymbol{k}$. Models of MHD turbulence predict the power spectra for these different types of modes as a function of the magnitude and orientation (with respect to the background magnetic field) of the wavevector $\boldsymbol{k}$ (Cho et al. 2003; Elmegreen & Scalo 2004; Schekochihin et al. 2009; Brandenburg & Lazarian 2013). A vigorous effort, based on analytic arguments and numerical simulations, is afoot to nail down these predictions, with much of the effort tracing back to classic work by Iroshnikov (1964) and Kraichnan (1965) and later Shebalin et al. (1983), and more recently, for example, Goldreich & Sridhar (1995); Lithwick & Goldreich (2001), and Cho & Lazarian (2002).

Another view of the anisotropy of MHD turbulence comes via studies of the filamentary structures in the cold neutral medium (CNM) of the ISM. Herschel has attracted attention to the filamentary structure of dust (André et al. 2010; Miville-Deschenes et al. 2010; Molinari et al. 2010). Other observations support this link between linear-polarization structures and turbulent, anisotropic CNM (Kalberla & Kerp 2016). In simulations, spherical clumps preferentially condense into filaments along magnetic field lines; the strain in the magnetic field is seen to play an essential role in creating filamentary density structures aligned with the local field orientation (Hennebelle 2013; Inoue & Inutsuka 2016).

The Planck Collaboration observed that correlations of filamentary structures (Adam et al. 2016b; Ade et al. 2016) with fluctuations in the magnetic field orientation could account for the observed ratio. The Planck Collaboration made further contact with MHD turbulence models for the ISM in Ade et al. (2015b) and Aghanim et al. (2016) through measurement of distributions of polarization magnitudes and orientation angles. Planck (Adam et al. 2016b) uses the dust maps at 353 GHz to show that polarization correlates with the orientation of extended structures in the intensity. This is interpreted as indicating that matter structures of the ISM are preferentially aligned with the magnetic field line. Similarly, Clark et al. (2015) find a correlation between the orientation angles of structures in the Planck 353 GHz intensity map and maps of diffuse neutral hydrogen. For example, MHD simulations suggest that the alignment between dust filaments and magnetic field lines arises from turbulent shear, which stretches both the CNM and the magnetic field (Inoue & Inutsuka 2016). This work does not, however, explain how the relevant density–magnetic field correlations arise in terms of the fundamental modes of fluctuations in the magnetized fluid. There is thus room to make clearer contact with theoretical models for a magnetized fluid.

Below we calculate the E- and B-mode amplitudes induced by slow, fast, and Alfvén waves, and also for longitudinal and transverse waves, for different directions of the background magnetic field with respect to the line of sight and for different wavevectors $\boldsymbol{k}$. This theoretical framework allows one to draw a quantitative connection between MHD waves in the ISM and the observed polarization pattern. Since the $EE/BB \simeq 2$ ratio seems to be relatively generic across the sky, it must arise after averaging over all magnetic field orientations. We thus then calculate the E and B power-spectrum amplitudes, as well as the temperature-polarization cross-correlation, obtained after averaging over all magnetic field and $\boldsymbol{k}$ orientations. We provide results as a function of the ratio $\beta \equiv P_g/P_H$ of the gas and magnetic field pressures, P_g and P_H, respectively. Although the true ISM is observed to be a multicomponent medium (e.g., Heiles & Troland 2003) that is highly anisotropic and characterized by filamentary structure, in this work we consider a toy model in which dust traces a single component of plasma. We also include a parameter λ that describes the anisotropy of the slow, fast, and Alfvén waves resulting from MHD turbulence. These calculations can then be used to assess the validity of any particular model for MHD turbulence specified by the power in the slow, fast, and Alfvén waves, and the anisotropy of that power.

We caution that our framework fails (or could fail) to describe a multi-phase medium in several ways. In particular, it is true that all fluid displacements can be decomposed into the three wave modes since they are a complete basis. However, our framework is perturbative, so it should not be expected to work quantitatively for highly dense structures. Considering that the density contrast between the cold and warm gas phases of the ISM varies by up to two orders of magnitude, we have made a gross over-simplification in treating the ISM as a single, linearly perturbative fluid. Consequently, the physical interpretations of that single-fluid basis as wave modes are not correct in a multi-phase medium. And finally, we have assumed the dust, magnetic field, and gas are all perfectly tied to each other.

Our results suggest that for $\beta \gtrsim 1$, the observed *EE/BB* ratio and temperature-polarization cross-correlation can be explained only if the power in fast waves greatly exceeds that in slow/Alfvén waves, and moreover, only if those fast waves have a nearly isotropic spectrum. The observations can also be explained in a low-β (strong-field) plasma with an additional contribution from an anisotropic spectrum of Alfvén waves, but only if the slow waves are very anisotropic or somehow suppressed. We thus infer that the observed *EE/BB* and *TE* are in tension with expectations from MHD turbulence. The apparent scale invariance of the *EE/BB* ratio over the range $\ell \simeq 30$–600 and the spectral index of the fluctuations—which disagrees with that expected from turbulence and that seen in electron-density fluctuations on smaller scales (Armstrong et al. 1995)—are also not easily accommodated by current MHD turbulence models.

In the context of our limited model, we thus speculate that the ∼0.1–30 pc length scales probed by *Planck* may overlap the outer scale of turbulence, the largest distance scale on which turbulence is driven. We then develop a simple phenomenological model, based on random displacements of a magnetized fluid, that accounts for $EE/BB \simeq 2$ and $TE > 0$. We further show that the *TE* correlation and large *EE/BB* are primarily a consequence of the longitudinal, rather than transverse, modes in the random-displacement field. We surmise that this may indicate something about the physics—perhaps stellar winds, protostellar outflows, supernovae (Lacki 2013; Padoan et al. 2016), or Galactic spiral shocks (Kim et al. 2006)—that drives small-scale turbulence in the ISM.

Directions for future related research include improved measurement of the *Planck TE* cross-correlation coefficient calculated here; studies of the variation of *EE/BB* and *TE* (that arise from variations in the background magnetic field orientation) across the sky; searches for local departures from statistical isotropy that arise for the same reason; and more precise measurements of the ℓ dependence of the dust power spectra. Moreover, as discussed below, we assume here that the dust density traces the plasma density, a hypothesis that we argue is reasonable, although one whose validity requires further investigation. There are thus further studies that should be done—including the frequency dependence of the *E/B/T* maps, cross-correlation with synchrotron-polarization maps, and perhaps cross-correlation with polarized-starlight surveys—to further test this hypothesis. Finally, a better understanding of the physics responsible for polarized dust emission may also aid in the development of algorithms to separate the CMB-polarization signal from polarized dust emission (Dunkley et al. 2009) and thus help advance the quest for inflationary gravitational waves (Kamionkowski

et al. 1997a; Seljak & Zaldarriaga 1997; Kamionkowski & Kovetz 2016).

Such developments must not necessarily await the next flagship satellite mission: there are prospects for considerable improvements in dust-polarization maps on small patches of sky with suborbital experiments (Kovetz & Kamionkowski 2016) such as BLASTPol (Fissel et al. 2010), BFORE (Niemack et al. 2015), TOLTEC (G. Wilson 2016, private communication), or PILOT (Misawa et al. 2014). Measurements of Galactic synchrotron and/or dust-polarization on larger angular scales will be improved, for example, with CLASS (Essinger-Hileman et al. 2014) or LiteBird (Matsumura et al. 2013). Analyses similar to those that we discuss can also be applied to maps of starlight polarization (Goodman et al. 1990; Heiles 1996; Fosalba et al. 2002) or neutral-hydrogen filaments (Clark et al. 2014, 2015), although the polarization strength is small, and the sparse sampling and the range of distances to stars complicates the *E/B* mode analysis. Moreover, similar analyses may be employed to understand, with dust-polarization maps, magnetic field structure in specific molecular clouds (Pelkonen et al. 2007; Kataoka et al. 2012; Koch et al. 2013; Soler et al. 2013).

This paper is organized as follows. In Section 2 we review the *E/B* decomposition of a polarization map. We review the relevant properties of MHD waves in Section 3. Section 4 calculates the *E* and *B* amplitudes that arise from slow, fast, and Alfvén waves. Section 5 discusses calculation of the power spectra. Section 6 presents the results of the calculations. In Section 7 we provide some possible interpretations of the data in terms of MHD turbulence models and also discuss the tension with expectations from favored MHD turbulence models. We therefore consider, in Section 8, a simple phenomenological model of random displacements in a magnetized fluid that results in $EE/BB \simeq 2$ and $TE > 0$. We then conclude and enumerate several possible research directions in Section 9.

To avoid confusion with the *E/B* decomposition of polarization maps, we use $\boldsymbol{H}$ to denote the magnetic field. The c.g.s. system of units is used.

2. Review of the *E/B* Decomposition of a Polarization Map and Projection Effects

Here we recall some basic properties of the decomposition of a polarization map into *E* and *B* modes, and the way in which three-dimensional emitting structures appear on the two-dimensional sky. We consider a map of the linear polarization on a patch of sky sufficiently small to be assumed flat, and of a solid angle Ω. We assume the emission to be optically thin, which is a good approximation at microwave frequencies.

The polarization is specified in terms of Stokes parameters $Q(\boldsymbol{\theta})$ and $U(\boldsymbol{\theta})$, measured with respect to some $\hat{\boldsymbol{\theta}}_x$–$\hat{\boldsymbol{\theta}}_y$ axes in the plane of the sky, which can then be written as a complex polarization $\Pi(\boldsymbol{\theta}) = Q(\boldsymbol{\theta}) + iU(\boldsymbol{\theta})$.[4] The map is equivalently represented by the Fourier transform

$$\tilde{\Pi}(\boldsymbol{\ell}) = \int_\Omega d^2\boldsymbol{\theta}\, \Pi(\boldsymbol{\theta}) e^{-i\boldsymbol{\ell}\cdot\boldsymbol{\theta}}. \quad (1)$$

The density of Fourier modes in the two-dimensional $\boldsymbol{\ell}$-plane is $\Omega/(2\pi)^2$.

[4] In the CMB literature this is often written $P(\boldsymbol{\theta})$, but here we write Π to avoid confusion with the 3D power spectrum.

The Stokes parameters, and the complex polarization, are not rotational invariants; under a rotation of the coordinate axes by an angle α, the polarization transforms as $\Pi \to \Pi e^{2i\alpha}$. The polarization field can be represented in terms of rotational invariants *E* and *B*. In Fourier space these are

$$(\tilde{E} + i\tilde{B})(\boldsymbol{\ell}) = (\tilde{Q} + i\tilde{U})(\boldsymbol{\ell}) e^{-2i\psi_\ell} \quad (2)$$

(Kamionkowski et al. 1997a, 1997b; Seljak & Zaldarriaga 1997; Seljak 1997; Zaldarriaga & Seljak 1997; Cabella & Kamionkowski 2004; Kamionkowski & Kovetz 2016), where ψ_ℓ is the angle that $\boldsymbol{\ell}$ makes with $\hat{\boldsymbol{\theta}}_x$, i.e., $\tan\psi_\ell = \ell_y/\ell_x$. The power spectra measured by Planck are then $C_\ell^{EE} = \langle|\tilde{E}(\boldsymbol{\ell})|^2\rangle/\Omega$ and $C_\ell^{BB} = \langle|\tilde{B}(\boldsymbol{\ell})|^2\rangle/\Omega$, where the average is over all $\boldsymbol{\ell}$ of magnitude ℓ.[5]

The observed polarization signal Π is typically measured in units of $\mu\mathrm{K}_{\mathrm{CMB}}$, and its angular power spectra $C_\ell^{EE/BB}$ have units of $\mu\mathrm{K}_{\mathrm{CMB}}^2$. However, for optically thin emission, the polarization is related to the polarized emissivity ε_Π via

$$\Pi(\boldsymbol{\theta}) = \int_0^\infty \varepsilon_\Pi(r\hat{\boldsymbol{n}}(\boldsymbol{\theta}))\, dr, \quad (3)$$

where $\hat{\boldsymbol{n}}(\boldsymbol{\theta})$ is the three-dimensional unit vector in the direction corresponding to angular position $\boldsymbol{\theta}$. The emissivity ε_Π (and its components, ε_Q and ε_U) have units of $\mu\mathrm{K}_{\mathrm{CMB}}\,\mathrm{pc}^{-1}$, and its three-dimensional power spectra $P_{\varepsilon,EE}(\boldsymbol{k})$ and $P_{\varepsilon,BB}(\boldsymbol{k})$ have units of $[\varepsilon_P^2] \times [\mathrm{volume}]$, or $\mu\mathrm{K}_{\mathrm{CMB}}^2\,\mathrm{pc}$.

For small angles or $\ell \gg 2$, the relation of three-dimensional and two-dimensional power spectra is usually obtained via the Limber approximation. This begins with breaking the line of sight integral, Equation (3), into a series of boxes along the line of sight of width Δr_i. In each box, the emissivity can be Fourier-transformed to $\tilde{\varepsilon}_\Pi(\boldsymbol{k})$:

$$\tilde{\varepsilon}_\Pi(\boldsymbol{k}) = \int_V \varepsilon_\Pi(\boldsymbol{x}) e^{-i\boldsymbol{k}\cdot\boldsymbol{x}}\, d^3\boldsymbol{x} \;\leftrightarrow\; \varepsilon_\Pi(\boldsymbol{x}) = \sum_{\boldsymbol{k}} \tilde{\varepsilon}_\Pi(\boldsymbol{k}) e^{i\boldsymbol{k}\cdot\boldsymbol{x}}, \quad (4)$$

where the Fourier wavevector $\boldsymbol{k}$ has (i) a transverse component $\boldsymbol{k}_\perp$ with a density of modes $r^2\Omega/(2\pi)^2$, and (ii) a line of sight component $k_\parallel = 2\pi n/\Delta r_i$ with $n \in \mathbb{Z}$. The volume of the box is $V = r^2\Omega\Delta r_i$. These transformed quantities satisfy

$$\begin{aligned}\langle\tilde{\varepsilon}_E^*(\boldsymbol{k})\tilde{\varepsilon}_E(\boldsymbol{k}')\rangle &= (2\pi)^3\delta^{\mathrm{D}}(\boldsymbol{k}-\boldsymbol{k}')P_{\varepsilon,EE}(\boldsymbol{k}) \\ &= r^2\Omega\Delta r_i\, \delta^{\mathrm{K}}_{\boldsymbol{k},\boldsymbol{k}'} P_{\varepsilon,EE}(\boldsymbol{k}). \end{aligned} \quad (5)$$

Only the transverse ($n = 0$ or $k_\parallel = 0$) modes, i.e., those with $\boldsymbol{k}$ in the plane of the sky, survive radial integration. They relate to the projected polarization via

$$\tilde{\Pi}(\boldsymbol{\ell}) = \sum_i \frac{1}{r^2}\tilde{\varepsilon}_\Pi(\boldsymbol{k} = \boldsymbol{\ell}/r), \quad (6)$$

where the $1/r^2$ comes from the transformation from $d^2\boldsymbol{\theta}$ to $d^2\boldsymbol{x}_\perp$ in the Fourier integral (see Equation (1)), and from Equation (5)

[5] The factor of Ω arises from the density of Fourier modes; the "usual" equation would read $\langle\tilde{E}^*(\boldsymbol{\ell})\tilde{E}(\boldsymbol{\ell}')\rangle = (2\pi)^2\delta^{\mathrm{D}}(\boldsymbol{\ell}-\boldsymbol{\ell}')C_\ell^{EE}$, where δ^{D} is the Dirac δ-function. For a density of modes $\Omega/(2\pi)^2$, we have $(2\pi)^2\delta^{\mathrm{D}}(\boldsymbol{\ell}-\boldsymbol{\ell}') \to \Omega\delta^{\mathrm{K}}_{\ell,\ell'}$, where δ^{K} is the Kronecker δ-symbol.

the two-dimensional power spectrum is

$$C_\ell^{EE} \approx \sum_i \frac{P_{\varepsilon,EE}(k=\ell/r)}{r^2}\Delta r_i \approx \int_0^{r_{\rm max}} \frac{P_{\varepsilon,EE}(k=\ell/r)}{r^2}\,dr, \tag{7}$$

where $r_{\rm max}$ is the maximum distance from which dust emission is seen. Equation (7) is the Limber equation, as commonly used in cosmology. The derivation contains two subtle assumptions: (i) each box can be treated as a statistically homogeneous medium; and (ii) when squaring Equation (6) and taking the expected value, we can neglect correlations between different boxes $i \neq j$.

In most of this paper, we will focus our attention on the ratios of the power spectra, $P_{\varepsilon,EE}(k)/P_{\varepsilon,BB}(k)$, or correlation coefficients between the E-mode and temperature $r = P_{\varepsilon,TE}(k)\big/[P_{\varepsilon,TT}(k)P_{\varepsilon,EE}(k)]^{1/2}$. It is easily seen from Equation (7) that the corresponding ratio in the power spectrum, C_ℓ^{BB}/C_ℓ^{EE}, is a suitably weighted average of $P_{\varepsilon,EE}(k)/P_{\varepsilon,BB}(k)$ along the line of sight. Therefore, in attempting to explain the observed *EE/BB* ratio, we focus on the three-dimensional power spectrum. When we consider the scale dependence of the polarization power spectrum, we will have to return to the full version of Equation (7).

3. Magnetohydrodynamic Waves

A compressible magnetized plasma can, in the MHD limit, carry three different types of waves, linear combinations of the two transverse-vector components of the magnetic field $\boldsymbol{H}$ (since the requirement $\boldsymbol{\nabla}\cdot\boldsymbol{H}=0$ removes the longitudinal-vector degree of freedom) and the plasma-density degree of freedom. Here we briefly reprise the properties, relevant for this work, of these three MHD waves, which are classified into Alfvén, slow, and fast modes.

We consider a magnetized plasma at rest with a homogeneous magnetic field $\boldsymbol{H}_0$ and then consider small perturbations parametrized in terms of a magnetic field perturbation $\delta\boldsymbol{H}(\boldsymbol{x},t)$ and plasma velocity $\boldsymbol{v}(\boldsymbol{x},t)$. In the MHD limit, the perturbation, velocity, and background field are related (in Fourier space) by

$$\omega\delta\boldsymbol{H} = -\boldsymbol{k}\times(\boldsymbol{v}\times\boldsymbol{H}_0), \tag{8}$$

where here $\delta\boldsymbol{H}$ and $\boldsymbol{v}$ are taken to be the magnetic field and velocity amplitudes of this particular Fourier mode.

3.1. Alfvén Waves

The Alfvén wave has a velocity perpendicular to both $\boldsymbol{k}$ and $\boldsymbol{H}$, and it has a dispersion relation $\omega = \pm ak\cos\alpha$, where $a = H_0(4\pi\rho)^{-1/2}$ is the Alfvén speed (and ρ the plasma mass density), and $\cos\alpha = \hat{\boldsymbol{k}}\cdot\hat{\boldsymbol{H}}_0$. For this wave, $\delta\boldsymbol{H} = \pm H_0(\boldsymbol{v}/a)$. The continuity equation, $(\partial n/\partial t) + \nabla\cdot(n\boldsymbol{v}) = 0$, provides a relation, $(\delta n/n_0) = \boldsymbol{k}\cdot\boldsymbol{v}/\omega$, between the fractional density perturbation $(\delta n/n_0)$ and the velocity. Since $\boldsymbol{k}\perp\boldsymbol{v}$ in the Alfvén wave, these waves have no associated density perturbation. We thus write,

$$\delta\boldsymbol{H} = -\frac{vH_0}{a}\hat{\boldsymbol{a}}, \tag{9}$$

where $\hat{\boldsymbol{a}} \equiv \hat{\boldsymbol{k}}\times\hat{\boldsymbol{H}}/\sin\alpha$ is the unit vector perpendicular to $\boldsymbol{k}$ and $\boldsymbol{H}$.

3.2. Slow/Fast Waves

The slow and fast waves both have magnetic field perturbations in a direction $\hat{\boldsymbol{\theta}} = -\hat{\boldsymbol{k}}\times(\hat{\boldsymbol{k}}\times\hat{\boldsymbol{H}})/\sin\alpha$ perpendicular to $\hat{\boldsymbol{k}}$ and $\hat{\boldsymbol{a}}$. The slow wave has a displacement in the direction $\hat{\boldsymbol{\xi}}_s \propto \cos\alpha\hat{\boldsymbol{H}} + \zeta_s\sin\alpha\hat{\boldsymbol{k}}_\perp$, where $\hat{\boldsymbol{k}}_\perp$ is a unit vector in the $\boldsymbol{k}$–$\boldsymbol{H}$ plane perpendicular to $\hat{\boldsymbol{H}}$, and the fast wave is in the orthogonal direction, $\hat{\boldsymbol{\xi}}_f \propto \zeta_f\cos\alpha\hat{\boldsymbol{H}} + \sin\alpha\hat{\boldsymbol{k}}_\perp$. Here,

$$\begin{aligned}\zeta_s &= \frac{1-\sqrt{D}-\beta/2}{1+\sqrt{D}+\beta/2}\cot^2\alpha,\\ \zeta_f &= \frac{1-\sqrt{D}+\beta/2}{1+\sqrt{D}-\beta/2}\tan^2\alpha,\end{aligned} \tag{10}$$

where $D = (1+\beta/2)^2 - 2\beta\cos^2\alpha$, and $\beta = P_g/P_H$ is the ratio of gas pressure to magnetic field pressure. In the strong-field limit $\beta\to 0$, and $\beta\to\infty$ in the weak field limit.

From Equation (8) it follows that for the slow wave,

$$\delta\boldsymbol{H} = \frac{kvH_0}{\omega}\frac{\zeta_s\sin\alpha}{(\cos^2\alpha+\zeta_s^2\sin^2\alpha)^{1/2}}\hat{\boldsymbol{\theta}}, \tag{11}$$

and for the fast wave,

$$\delta\boldsymbol{H} = \frac{kvH_0}{\omega}\frac{\sin\alpha}{(\zeta_f^2\cos^2\alpha+\sin^2\alpha)^{1/2}}\hat{\boldsymbol{\theta}}, \tag{12}$$

where v is the magnitude of the fluid velocity. For the Alfvén wave, the relationship between the magnitudes of the magnetic field and velocity perturbations is independent of the orientation of $\boldsymbol{k}$ (cf. Equation (9)). The same is not true, however, for the slow/fast waves. In addition to the explicit α dependence in Equations (11)–(12), there is also an α dependence in $\zeta_{s,f}$ and also in the dispersion relations,

$$\left(\frac{\omega}{k}\right)^2 = \frac{a^2}{2}(1+\beta/2)\left[1\pm\left(1-\frac{2\beta\cos^2\alpha}{(1+\beta/2)^2}\right)^{1/2}\right], \tag{13}$$

for the fast (plus sign) and slow (minus sign) waves.

The fractional density perturbation is then found from the continuity equation to be, for the slow wave,

$$\frac{\delta n}{n_0} = \frac{kv}{\omega}\frac{(\cos^2\alpha+\zeta_s\sin^2\alpha)}{(\cos^2\alpha+\zeta_s^2\sin^2\alpha)^{1/2}}, \tag{14}$$

and for the fast wave,

$$\frac{\delta n}{n_0} = \frac{kv}{\omega}\frac{(\zeta_f\cos^2\alpha+\sin^2\alpha)}{(\zeta_f^2\cos^2\alpha+\sin^2\alpha)^{1/2}}. \tag{15}$$

The final relations then are those between the magnetic field perturbation and the density perturbation, and the magnetic field perturbation and the velocity perturbation. They are, for the slow wave,

$$\frac{\delta n}{n_0} = \frac{|\delta\boldsymbol{H}|}{H_0}(\cos^2\alpha+\zeta_s\sin^2\alpha)/(\zeta_s\sin\alpha) \equiv \frac{|\delta\boldsymbol{H}|}{H_0}g_s(\alpha), \tag{16}$$

$$\frac{|\delta\boldsymbol{H}|}{H_0} = \frac{k}{\omega}\frac{\zeta_s\sin\alpha}{(\cos^2\alpha+\zeta_s^2\sin^2\alpha)^{1/2}}|\boldsymbol{v}| \equiv |\boldsymbol{v}|h_s(\alpha), \tag{17}$$

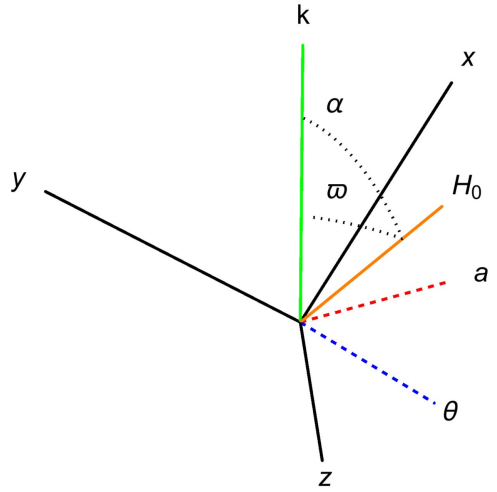

Figure 1. The coordinate axes and relevant vectors are shown. The locations of $\boldsymbol{H}_0$ and $\boldsymbol{k}$ are shown by the orange and green lines, and $\boldsymbol{a}$ and $\hat{\theta}$ are shown by the dashed red and blue lines, respectively. The coordinates α and ϖ relative to $\boldsymbol{k}$ are also indicated. Recall that the line of sight is along the z direction.

and for the fast wave,

$$\frac{\delta n}{n_0} = \frac{|\delta \boldsymbol{H}|}{H_0}(\zeta_f \cos^2\alpha + \sin^2\alpha)/\sin\alpha \equiv \frac{|\delta \boldsymbol{H}|}{H_0} g_f(\alpha), \quad (18)$$

$$\frac{|\delta \boldsymbol{H}|}{H_0} = \frac{k}{\omega}\frac{\sin\alpha}{(\zeta_f^2\cos^2\alpha + \sin^2\alpha)^{1/2}}|\boldsymbol{v}| \equiv |\boldsymbol{v}| h_f(\alpha). \quad (19)$$

In the case of the Alfvén wave, as seen in Equation (9), we have $|\delta \boldsymbol{H}|/H_0 = |\boldsymbol{v}|/a \equiv |\boldsymbol{v}| h_a$. These relations allow us to determine the E- and B-mode powers under different assumptions about the power spectra for the different MHD waves.

4. E and B Modes Induced by the Slow, Fast, and Alfvén Waves

4.1. E and B Amplitudes from a Single Fourier Mode

Take the line of sight to be along the z axis and the background field $\boldsymbol{H}_0 = H_0(\sin\theta, 0, \cos\theta)$ in the x–z plane at an angle θ from the line of sight. Consider a perturbation of wavevector $\boldsymbol{k} = k\hat{\boldsymbol{k}} = k(\cos\psi, \sin\psi, 0)$ in the x–y plane of the sky (as the two-dimensional projections of other modes will experience a Limber suppression) oriented at an angle ψ with respect to the x axis. The angle α between $\boldsymbol{k}$ and $\boldsymbol{H}$ is then given by $\cos\alpha = \sin\theta\cos\psi$, as illustrated in Figure 1.

We observe a two-dimensional projection of an emitting volume, and the polarized emission is assumed to have the form

$$\varepsilon_P = \varepsilon_Q + i\varepsilon_U = AnH^\gamma (H_x + iH_y)^2, \quad (20)$$

where γ is an exponent that is equal to -2 if the dust alignment is independent of the magnetic field strength, n is proportional to the dust density (and has a constant background value n_0). Here $A < 0$ is a constant; its value is taken to be negative so that the polarization is perpendicular to the magnetic field (Chandrasekhar & Fermi 1953). The sign of A will be significant for the temperature-polarization cross-correlation below. The polarization fluctuations are

$$\delta\varepsilon_P = An_0 H_0^{2+\gamma}\left[2\sin\theta\,\frac{\delta H_x + i\delta H_y}{H_0} + \gamma\sin^2\theta\,\frac{\delta H}{H_0} + \sin^2\theta\,\frac{\delta n}{n_0}\right], \quad (21)$$

where here $\delta H = \sin\theta\delta H_x + \cos\theta\delta H_z$. For a given Fourier mode of wavevector $\boldsymbol{k}$ transverse to the line of sight in a box of radial width Δr, the E and B modes will appear in wavevector $\boldsymbol{\ell} = \boldsymbol{k}r$, and will have the form:

$$\tilde{E} + i\tilde{B} = An_0 H_0^{2+\gamma}\frac{\Delta r}{r^2}\,e^{-2i\psi}\left[2\sin\theta\,\frac{\delta\tilde{H}_x + i\delta\tilde{H}_y}{H_0} + \gamma\sin^2\theta\,\frac{\delta\tilde{H}}{H_0} + \sin^2\theta\,\frac{\delta\tilde{n}}{n_0}\right], \quad (22)$$

which can be decomposed into

$$\tilde{E} = An_0 H_0^{2+\gamma}\frac{\Delta r}{r^2}\left[2\sin\theta\cos 2\psi\frac{\delta\tilde{H}_x}{H_0} + 2\sin\theta\sin 2\psi\,\frac{\delta\tilde{H}_y}{H_0} + \gamma\sin^2\theta\cos 2\psi\,\frac{\delta\tilde{H}}{H_0} + \sin^2\theta\cos 2\psi\,\frac{\delta\tilde{n}}{n_0}\right], \quad (23)$$

$$\tilde{B} = An_0 H_0^{2+\gamma}\frac{\Delta r}{r^2}\left[-2\sin\theta\sin 2\psi\,\frac{\delta\tilde{H}_x}{H_0} + 2\sin\theta\cos 2\psi\,\frac{\delta\tilde{H}_y}{H_0} - \gamma\sin^2\theta\sin 2\psi\,\frac{\delta\tilde{H}}{H_0} - \sin^2\theta\sin 2\psi\,\frac{\delta\tilde{n}}{n_0}\right]. \quad (24)$$

We now rewrite the magnetic field perturbations in terms of the two transverse-vector modes, those in the $\hat{\boldsymbol{a}}$ (the Alfvén wave) and $\hat{\boldsymbol{\theta}}$ (the slow and fast waves) directions:

$$\begin{aligned}(\delta\tilde{\boldsymbol{H}})_a &= \hat{\boldsymbol{a}}\delta\tilde{H}_a = \frac{\hat{\boldsymbol{k}}\times\hat{\boldsymbol{H}}}{\sin\alpha}\delta\tilde{H}_a \\ &= \frac{(\sin\psi\cos\theta,\ -\cos\psi\cos\theta,\ -\sin\psi\sin\theta)}{\sin\alpha}\delta\tilde{H}_a, \\ (\delta\tilde{\boldsymbol{H}})_p &= \hat{\boldsymbol{\theta}}\delta\tilde{H}_p = -\frac{\hat{\boldsymbol{k}}\times(\hat{\boldsymbol{k}}\times\hat{\boldsymbol{H}})}{\sin\alpha}\delta\tilde{H}_p \\ &= \frac{(\sin\theta\sin^2\psi,\ -\sin\theta\sin\psi\cos\psi,\ \cos\theta)}{\sin\alpha}\delta\tilde{H}_p, \end{aligned} \quad (25)$$

where $\delta\tilde{H}_a$ ("a" for Alfvén) and $\delta\tilde{H}_p$ ("p" for pseudo-Alfvén) are the magnetic field amplitudes for the two modes. These then translate to E and B modes,

$$\tilde{E} = An_0 H_0^{2+\gamma}\frac{\Delta r}{r^2}\left[-\sin 2\theta\frac{\sin\psi}{\sin\alpha}\frac{\delta\tilde{H}_a}{H_0} + \frac{\sin^2\theta[-2\sin^2\psi(1+\gamma\sin^2\alpha)+\gamma\sin^2\alpha]}{\sin\alpha}\frac{\delta\tilde{H}_p}{H_0} + \sin^2\theta\cos 2\psi\frac{\delta\tilde{n}}{n_0}\right], \quad (26)$$

$$\tilde{B} = An_0 H_0^{2+\gamma} \frac{\Delta r}{r^2} \Bigg[-\sin 2\theta \frac{\cos\psi}{\sin\alpha} \frac{\delta\tilde{H}_a}{H_0} - \frac{2\sin^2\theta \sin\psi\cos\psi(1+\gamma\sin^2\alpha)}{\sin\alpha} \frac{\delta\tilde{H}_p}{H_0} - \sin^2\theta \sin 2\psi \frac{\delta\tilde{n}}{n_0} \Bigg]. \quad (27)$$

For Alfvén waves, which have no associated density perturbation, we are already done. However, the fast and slow waves both have a density perturbation. The final step is thus to rewrite the p and n modes in terms of slow ("s") and fast ("f") modes using Equations (16) and (18). We then obtain

$$\begin{aligned}\tilde{E} &= An_0 H_0^{2+\gamma} \frac{\Delta r}{r^2} \Bigg[-\sin 2\theta \frac{\sin\psi}{\sin\alpha} \frac{\delta\tilde{H}_a}{H_0} + \sum_{i=s,f} \frac{\delta\tilde{H}_i}{H_0} \sin^2\theta \\ &\quad \times \left(\frac{[-2\sin^2\psi(1+\gamma\sin^2\alpha) + \gamma\sin^2\alpha]}{\sin\alpha} \right) \\ &\quad + g_i(\alpha)\cos 2\psi)] \equiv An_0 H_0^{2+\gamma} \frac{\Delta r}{r^2} \sum_{i=a,s,f} f_i^E(\theta,\psi) \frac{\delta\tilde{H}_i}{H_0} \\ &= An_0 H_0^{2+\gamma} \frac{\Delta r}{r^2} \sum_{i=a,s,f} f_i^E(\theta,\psi) h_i(\theta,\psi) |\boldsymbol{v}_i|, \end{aligned} \quad (28)$$

$$\begin{aligned}\tilde{B} &= An_0 H_0^{2+\gamma} \frac{\Delta r}{r^2} \Bigg[-\sin 2\theta \frac{\cos\psi}{\sin\alpha} \frac{\delta\tilde{H}_a}{H_0} \\ &\quad - \sum_{i=s,f} \frac{\delta\tilde{H}_i}{H_0} \sin^2\theta \sin 2\psi \left(\frac{(1+\gamma\sin^2\alpha)}{\sin\alpha} + g_i(\alpha) \right) \Bigg] \\ &\equiv An_0 H_0^{2+\gamma} \frac{\Delta r}{r^2} \sum_{i=a,s,f} f_i^B(\theta,\psi) \frac{\delta\tilde{H}_i}{H_0} \\ &= An_0 H_0^{2+\gamma} \frac{\Delta r}{r^2} \sum_{i=a,s,f} f_i^B(\theta,\psi) h_i(\theta,\psi) |\boldsymbol{v}_i|. \end{aligned} \quad (29)$$

The intermediate lines define the angular functions $f_i^{E,B}(\theta,\psi)$ which relate the polarization pattern to the magnetic field fluctuations, and the conversion into velocity fluctuations follows from Equations (17)–(19).

4.2. Temperature Fluctuations

The brightness temperature of the dust (synchrotron) emission is also provided, as a function of position on the sky, by *Planck* (Ade et al. 2015c; Adam et al. 2016a; *WMAP*, Page et al. 2007). Since the brightness temperature of dust emission is proportional to the dust density, temperature fluctuations arise from fluctuations δn in the dust density. The fractional intensity or temperature perturbation is thus,

$$\frac{\delta\epsilon_T}{\bar{\epsilon}_T} = c\frac{\delta n}{n_0}, \quad (30)$$

and projected through a box of width Δr we have

$$\tilde{T}(\boldsymbol{\ell}) = c\bar{\epsilon}_T \frac{\Delta r}{r^2} \frac{\delta\tilde{n}(\boldsymbol{k})}{n_0}. \quad (31)$$

We expect $c = 1$ for thermal dust emission since the physical temperature of the dust grains does not depend on the gas density (it is set by radiative equilibrium). Other dust emission mechanisms, e.g., spinning dust, may depend in a complicated way on the local gas density (e.g., Draine & Lazarian 1998; Ali-Haimoud et al. 2009) and hence for these we may have $c \neq 1$. Note, however, that our focus is on the *TE* cross-correlation coefficient, where c cancels out.

Written in terms of the wave modes, we find

$$\tilde{T}(\boldsymbol{\ell}) = c\bar{\epsilon}_T \frac{\Delta r}{r^2} \frac{\delta\tilde{n}}{n_0} = c\bar{\epsilon}_T \frac{\Delta r}{r^2} \sum_{i=s,f} g_i(\alpha) h_i(\alpha) |\boldsymbol{v}_i|. \quad (32)$$

Note that the Alfvén modes do not yield any density perturbations, and hence do not contribute to $\tilde{T}$.

5. Calculations of Power Spectra

We now calculate the power in E and B modes contributed by the three different types of waves. Strictly speaking, we calculate the contribution to the E- and B-mode powers at a given 3D wavenumber k. The observed 2D E- and B-mode powers, as a function of multipole ℓ, are then obtained from the Limber equation, which sums the contributions of wavenumbers $k = \ell/r$, from a range of distances r, to a given ℓ. If, however, the *EE/BB* ratio is scale-independent (as we assume here and as is consistent with the measurements), then the *EE/BB* ratio we calculate will also be that in the observed 2D power spectrum. Similar remarks apply to the *TE* correlation.

5.1. Parametrization of Power Anisotropies in the MHD Waves

Since the background magnetic field $\boldsymbol{H}_0$ provides a preferred direction, the power spectra for the three types of MHD waves are not expected to be isotropic, but should, rather, have some $\cos\alpha$ dependence (Shebalin et al. 1983; Goldreich & Sridhar 1995). Here we parametrize the anisotropy as

$$P_i(k,\cos\alpha) \equiv \left\langle \left| \frac{\delta\boldsymbol{H}_i}{H_0} \right|_{\boldsymbol{k}}^2 \right\rangle = P_i(k)[h_i(\alpha)]^2 F_\lambda(\cos\alpha), \quad (33)$$

with

$$F_\lambda(\mu) = \begin{cases} (\mu^2)^\lambda, & \text{if} \quad \lambda \geqslant 0, \\ (1-\mu^2)^{-\lambda}, & \text{if} \quad \lambda \leqslant 0. \end{cases} \quad (34)$$

We work with power spectra for the magnetic field amplitudes, but have then defined, by virtue of the $h_{s,f}(\alpha)$ in Equation (33), the anisotropy $F_\lambda(\mu)$ relative to the velocity perturbation amplitude. We do so to make contact with the MHD literature, wherein wave amplitudes are usually specified in terms of the velocity. With our parametrization, for $\lambda = 0$ the velocity power is isotropic; for $\lambda > 0$ it is weighted in modes of wavevector $\boldsymbol{k}$ parallel to $\boldsymbol{H}_0$; and for $\lambda < 0$, the velocity power is weighted in modes perpendicular to $\boldsymbol{H}_0$.

5.2. The EE/BB Ratio

Given that the *EE/BB* ratio seems to be roughly 2 everywhere on the sky, any MHD explanation of the *EE/BB* ratio must provide this ratio after averaging over all magnetic field orientations, rather than rely on a specific orientation. There is also evidence that the angular average is warranted even along an individual line of sight: if the field direction were

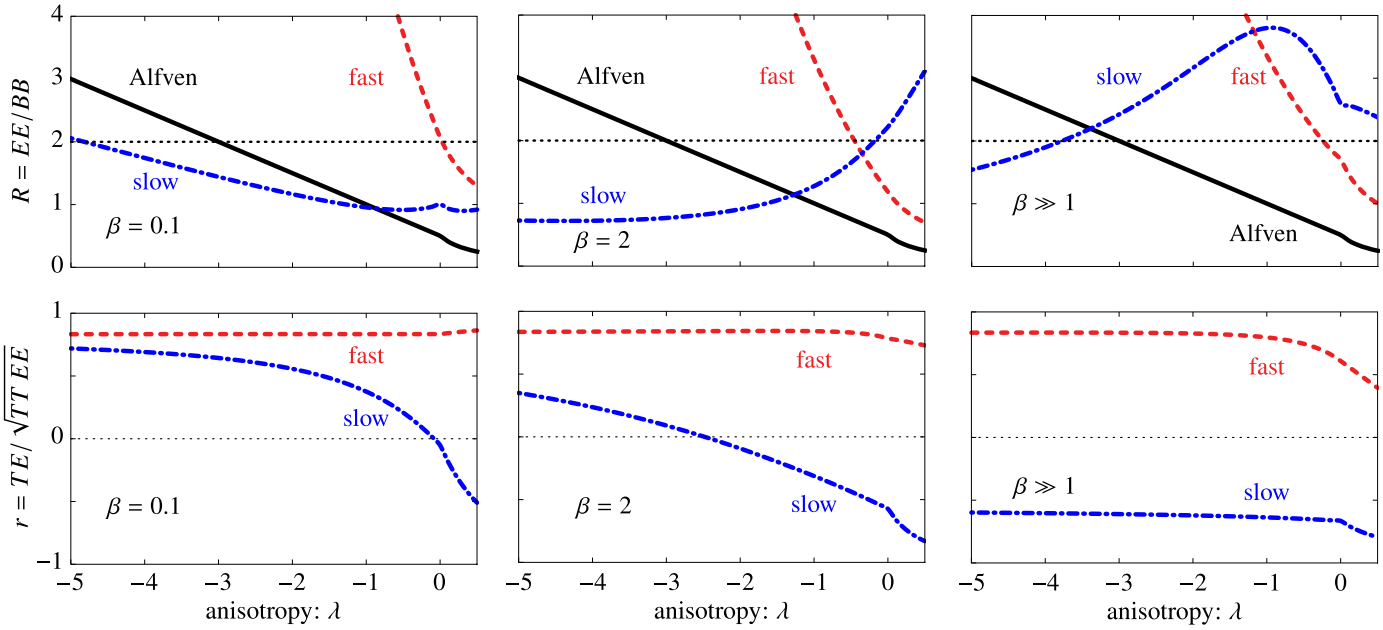

Figure 2. The *EE/BB* ratio and cross-correlation coefficient are shown as a function of the velocity power spectrum anisotropy index λ for $\beta = 0.1$, 2, and $\beta \gg 1$. The solid (black), long dashed (red), and dotted–dashed (blue) curves are for Alfvén, fast, and slow magnetosonic waves, respectively. The observed *EE/BB* ratio is indicated by the thin dashed (black) line in the upper panels. The positive cross-correlation *TE* is indicated by the thin dotted (black) line in the lower panels.

exactly constant along a given line of sight, then we would expect the fractional polarization for synchrotron radiation to be ∼75% (Rybicki & Lightman 1979). *Planck* obtains significantly lower values (see, e.g., Figure 22 in Ade et al. 2015d), suggesting a large dispersion in field direction even on a single line of sight.

We therefore calculate the ratios R of the angle-averaged E-mode and B-mode powers, induced by Alfvén, slow, and fast waves as a function of β and the anisotropy parameter λ. The desired ratio is obtained from

$$R_i(\beta,\,\lambda) = \frac{\int d\Omega [f_i^E(\theta,\,\psi) h_i(\alpha)]^2 F_\lambda(\cos\alpha)}{\int d\Omega [f_i^B(\theta,\,\psi) h_i(\alpha)]^2 F_\lambda(\cos\alpha)} \tag{35}$$

for $i = \{a, s, f\}$. Evaluation of the angular averages can be simplified by transforming to new angular coordinates α and ϖ, through $\cos\theta = \sin\alpha\cos\varpi$, $\sin\theta\sin\psi = \sin\alpha\sin\varpi$, and $\sin\theta\cos\psi = \cos\alpha$. These then are polar coordinates for the location of $\boldsymbol{H}_0$ about the k axis, rather than the z axis, as seen in Figure 1. We then integrate over $d\Omega = \sin\alpha\, d\alpha\, d\varpi$.

5.3. The Temperature-polarization Cross-correlation

Temperature fluctuations will arise from fluctuations in the density field, in accordance with Equation (32). The Alfvén modes do not contribute to temperature fluctuations. The slow and fast modes, however, should set up a correlation between the temperature and E-mode polarization. (The *TB* and *EB* cross-correlations vanish after averaging over angles.) The relative amplitudes of the polarization and temperature fluctuations depend on a polarization fraction and the constant c, so we work instead with a cross-correlation coefficient,

$$r_i(\lambda) = \frac{\int d\Omega [g_i(\alpha) h_i(\alpha)][f_i^E(\theta,\,\psi) h_i(\alpha)] F_\lambda(\cos\alpha)}{\sqrt{\int d\Omega [g_i(\alpha) h_i(\alpha)]^2 F_\lambda(\cos\alpha)}\sqrt{\int d\Omega [f_i^E(\theta,\,\psi) h_i(\alpha)]^2 F_\lambda(\cos\alpha)}}, \tag{36}$$

which corresponds to the ratio $TE/\sqrt{(TT)(EE)}$.

6. Results

The *EE/BB* ratio and cross-correlation coefficients are shown in Figure 2 for a strong magnetic field ($\beta = 0.1$), equipartition ($\beta = 2$), and weak field ($\beta \gg 1$). The two observational constraints, $EE/BB \simeq 2$ and $TE > 0$, can be satisfied by a nearly isotropic fast mode, for a wide range of β, or by a strongly anisotropic slow mode, with $\beta \lesssim 2$. More specifically, for a fast wave with $\beta = 0.1$, an isotropic spectrum ($\lambda = 0$) gives $EE/BB \simeq 2$ and cross-correlation coefficient $r \simeq 0.8$. For a slow wave with $\beta = 0.1$, too, a strongly anisotropic spectrum with $\lambda \sim -5$ gives $EE/BB \simeq 2$ and cross-correlation coefficient $r \simeq 0.7$. The constraints cannot be satisfied by a pure Alfvén wave, since this incompressible mode creates no intensity fluctuation and therefore no cross-correlation.

All the results illustrated assume $\gamma = -2$. However, we have also examined cases in which the polarization amplitude is correlated with the magnetic field, $\gamma > -2$, as well as the

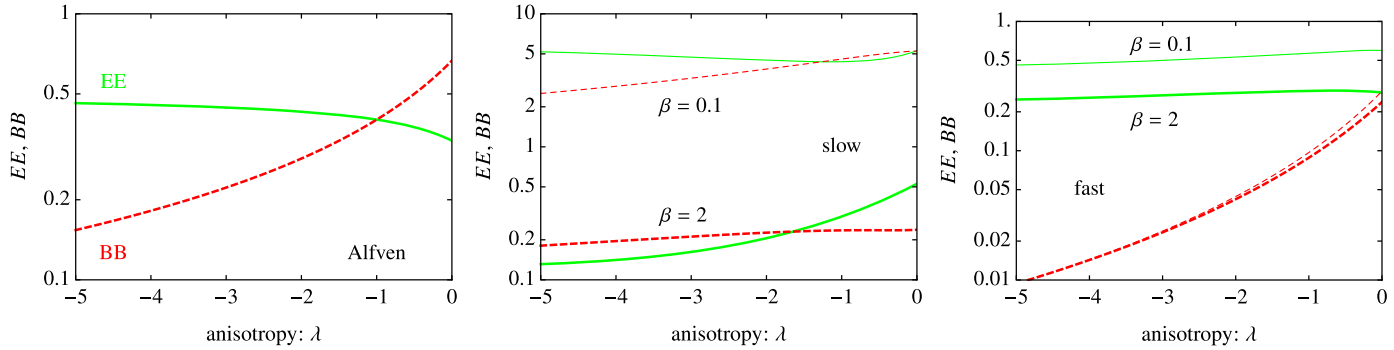

Figure 3. The power *EE* and *BB*, normalized to the power in velocity fluctuations, are shown for each of the velocity modes, for the representative cases $\beta = 2$ (thick lines) and $\beta = 0.1$ (thin lines). As labeled in the figures, solid (green) lines are *EE* and dashed (red) lines are *BB*.

inverse case, $\gamma < -2$. We find that our results for the *EE/BB* ratio and *TE* cross-correlation are not strongly sensitive to the dust alignment index in the range $-5/2 < \gamma < -3/2$.

7. Interpretations

In this section we try to make sense of the observations within the context of models for the ISM. We first consider MHD turbulence models and conclude that they are unlikely to provide the whole story. We then speculate that the *Planck* dust-polarization data may alternatively reflect the physics driving turbulence and/or involve new physics beyond that included in the MHD turbulence models we consider here.

7.1. MHD Turbulence?

7.1.1. EE/BB Ratio and TE Correlation

There are some important qualitative conclusions about MHD turbulence models that can be inferred from the observations $EE/BB \simeq 2$ and $TE > 0$. (Strictly speaking, the cross-correlation coefficient we calculate here has not yet been provided by *Planck*. We estimate it by comparing Figures 2 and B1 in Adam et al. (2016a) with Figure D1 in Ade et al. (2015c). There are uncertainties here: the cuts and assumptions that went into the latter figure are not necessarily those that went into the first two. Even so, we infer that the cross-correlation coefficient is reasonably large, and, more importantly, positive.) The models generally predict (Cho & Lazarian 2002) that: (a) slow/Alfvén waves should have similar power spectra; (b) the slow/Alfvén waves should preferentially populate modes perpendicular to the magnetic field ($\lambda < 0$ in our parlance); (c) the fast modes should be largely uncoupled from the slow/Alfvén modes; and (d) the fast modes should be nearly isotropic ($\lambda \simeq 0$).

We also need to consider the total *E*- and *B*-mode polarization powers contributed, for fixed angle-averaged velocity perturbation power, by each of the different types of MHD waves. These are plotted in Figure 3 for $\beta = 0.1$ and $\beta = 2$ (the results for $\beta \gg 1$ are similar to those for $\beta = 2$). For $\beta \gtrsim 1$, the polarization powers contributed by all three types of waves are roughly similar. However, the polarization power in slow modes scales inversely with β as $\beta \to 0$. Physically, this occurs because $(\omega/k) \to 0$ in this limit, indicating a vanishing restoring force. The fluid displacements, and thus density perturbations, become large. Thus, the *EE/BB* ratio and *TE* correlation will receive disproportionately large contributions from slow modes in a low-β plasma.

Looking at Figure 2, along with Figure 3, we see that the combination of the two constraints ($EE/BB \simeq 2$ and $TE > 0$) very seriously restricts the range of allowable models. There seem to be two possibilities: (1) a nearly isotropic spectrum of fast waves provides positive cross-correlation and $EE/BB \simeq 2$ for any β. A combination of slow/Alfvén waves is disallowed, on the other hand for $\beta \gtrsim 1$. Thus, the observations can be explained if $\beta \gtrsim 1$ and Alfvén/slow waves are somehow suppressed. (2) For $\beta \ll 1$, Alfvén waves can produce $EE/BB \simeq 2$ if sufficiently anisotropic, but they contribute nothing to *TE*. Slow modes can, if sufficiently anisotropic, also contribute $EE/BB \simeq 2$ and a positive *TE*. Given the theoretical expectation that the velocity power in slow and Alfvén waves is comparable, the slow waves will dominate at low β, and thus the anisotropy must be even greater to account for the observations.

The fettle of either of these MHD turbulence interpretations is damaged by the relative uniformity—as best can be determined—of the *EE/BB* ratio and *TE* correlation across the sky. The ISM is a complicated system that is likely to display considerable variation in the parameters β and λ and the relative contributions of strong/fast/Alfvén waves. While there are indeed pockets of the MHD turbulence parameter space that can account for the observed *EE/BB* and *TE*, these predictions will not be robust if there is considerable variation of β, λ, or the mix of slow/fast/Alfvén waves within the ISM.

7.1.2. Scale-dependent Anisotropy?

The observed power-law indexes for the ℓ dependences of the *EE* and *BB* power spectra agree to roughly a percent and are also very similar to those for the *TT* and *TE* power spectra (Adam et al. 2016a). As the figures indicate, the *EE/BB* ratios can depend quite a bit on the anistropy parameter λ. Thus, if the power anisotropy is scale-dependent, as expected in MHD turbulence (Goldreich & Sridhar 1995; Cho & Lazarian 2002), then one might expect to see different power-law indexes for *E* modes and *B* modes. Some caution should be used in drawing this conclusion since a given multipole-moment ℓ receives contributions from emission at a variety of line of sight distances r, and thus a variety of wavenumbers $k \sim \ell/r$. Still, we infer that there is no dramatic variation of the MHD power anisotropy over the ~0.1–30 pc length scales probed by *Planck*.

7.1.3. The Wavenumber Scaling

There is also a disparity between the spectral index $\nu \simeq 2.4$ measured for the *TE/EE/BB/TT* power spectra, $C_\ell \propto \ell^{-\nu}$, and the $\kappa \simeq 3.67$, in the three-dimensional power spectrum, $P(k) \propto k^{-\kappa}$ expected in MHD turbulence. The two exponents are related through the Limber equation, Equation (7). If the three-dimensional power spectrum is well-approximated by a single power law over the relevant distance scales, then the two-dimensional power spectrum C_ℓ will also be a power law, and moreover, with the same spectral index, $\nu = \kappa$. Given that the maximum distance from which we see dust emission (at least at high Galactic latitudes) is $r_{\rm max} \simeq$ 100–200 pc, the range of physical length scales probed by *Planck* measurements over $\ell \simeq$ 30–600 is roughly $L \sim$ 0.1–30 pc, where $L = 2\pi/k$.

7.2. An Outer Scale?

Turbulence is expected, however, to be described by a power law only below some outer distance scale L, or for wavenumber $k \gtrsim k_c \sim 2\pi L^{-1}$. Suppose, for example, that the power is $P(k) = 0$ for $k < k_c$ and $P(k) \propto k^{-\kappa}$ for $k > k_c$ (and with $q(r) =$ constant). In this case, we expect $C_\ell \propto \ell^{-1}$ for $\ell \ll \ell_c \equiv k_c r_{\rm max}$ and $C_\ell \propto \ell^{-\kappa}$ for $\ell \gg \ell_c$. It is conceivable that the apparent power-law index $\nu = 2.42$ approximates the scaling if the $\ell =$ 30–600 range over which the measurements are done contains the characteristic multipole $\ell_{\rm c}$ that separates the $C_\ell \propto \ell^{-1}$ low-ℓ behavior to the $C_\ell \propto \ell^{-\kappa} \sim \ell^{-3.67}$ behavior at higher ℓ. If so, then the outer scale is (taking $\ell_c \simeq 100$ and $r_{\rm max} \sim 100$ pc) $L \sim 10$ pc, a reasonable value and a value that is not too different from the ∼pc outer scale inferred from Faraday rotation and depolarization of extragalactic radio sources (Haverkorn et al. 2008). If the $\ell =$ 30–600 range does indeed correspond to the outer scale of turbulence, then guidance from MHD turbulence modeling about the power in slow/fast/Alfvén waves may be inappropriate. The observations may then have more to do with the large-scale physics—for example, stellar winds, protostellar outflows, supernovae (Lacki 2013; Padoan et al. 2016), or Galactic spiral shocks (Kim et al. 2006)—driving the turbulence, rather than the turbulence itself. In this case, the power-law behavior in C_ℓ should be only an approximation, and it should be found, with improved measurement, to be shallower at lower ℓ and steeper at higher ℓ.

If this interpretation is correct, then extrapolations of foreground power based on measurements at $30 \lesssim \ell \lesssim 600$ to lower ℓ may be overestimating the low-ℓ CMB foregrounds. If so, this will be good news (Kamionkowski & Kovetz 2016) for experiments, such as CLASS (Essinger-Hileman et al. 2014) and LiteBird (Matsumura et al. 2013), that go to low ℓ to seek this signal.

7.3. Warm/Neutral Transition

Another possibility is that the ISM is not described by the conventional MHD turbulence models. For example, it is well known that the ISM is a multi-phase medium. If there is some instability that allows transitions, for example, between a warm neutral phase and a cold neutral phase, then the ISM equation of state may be more complicated than that assumed in the standard MHD analysis (Norman & Ferrara 1996; Kritsuk & Norman 2002). If so, then the normal modes of the system may not necessarily correspond to the standard slow/fast/Alfvén waves—for any value of β—but rather consist of some other linear combinations of them.

7.4. Does Dust Trace Plasma?

The MHD approximation assumed here requires the magnetic field lines to be tied to the plasma, and the relations (Equations (16) and (18)) derived above are between the magnetic field and plasma-density perturbations. Strictly speaking, though, the quantity δn is the perturbation to the *dust* density. In deriving Equations (16) and (18), we have assumed that the dust and plasma are distributed in the same way. Although there are reasons to suspect that this assumption is largely valid, there are also indeed reasons to suspect that there may be dust-plasma relative motions of a magnitude large enough to affect our results, as we now discuss.

In a turbulent ISM, one generically expects that—at least on the large scales considered in this paper—dust should be well-mixed (see, e.g., Lazarian & Yan 2002). On small scales, however, the dust grains may not necessarily be well coupled to the gas. From a theoretical perspective, two major sources of coupling should be considered: collisional coupling with the atoms in the gas, and the gyromotion of charged grains in a magnetic field (Voelk et al. 1980; Draine 1985). The product of mean atomic velocity and the collisional drag time in a (mostly) neutral medium is

$$\bar{v}_{\rm H} t_{\rm drag} = \frac{a\rho_{\rm g}}{m_{\rm H} n_{\rm H}} = 5\, a_{-5} n_{\rm H}^{-1}\ {\rm pc}, \tag{37}$$

where we have used a grain density of $\rho_{\rm g} = 2.6$ g cm^{-3}, and written the grain radius in units of $a_{-5} = 10^{-5}$ cm, and the hydrogen density in units of cm^{-3}. If magnetic fields were neglected, we would expect the dust to trace the gas for sound waves of (reduced) wavelength $\lambda\!\!\!^{-} = k^{-1}$ larger than this scale. It is easily seen that for typical ISM distances $r \sim 100$ pc, the condition of dust–gas coupling through collisions should be violated at $\ell = kr \gtrsim 20 a_{-5}^{-1} n_{\rm H}$, i.e., well within the range of interest for the Planck dust-polarization maps. On the other hand, the gyromotion of charged grains in magnetic fields restricts the motion of dust grains in directions perpendicular to the magnetic field on a length scale of

$$v_{\rm A} t_{\rm L} = \frac{m_{\rm g} c}{\Phi a \sqrt{4\pi m_{\rm H} n_{\rm H}}} = 7 \times 10^{-5}\, a_{-5}^2 n_{\rm H}^{-1/2}\ {\rm pc}, \tag{38}$$

for grains with a potential $\Phi \sim 10\ V = 0.03$ statvolt generated by the photoelectric effect. Therefore, for Alfvén waves of (reduced) wavelength $\lambda\!\!\!^{-} = k^{-1}$ larger than this scale, we expect the dust to trace the plasma. Factors of β and trigonometric factors may appear in the coupling to the slow and fast MHD waves, but only for extreme values would we expect the Larmor coupling to fail.

A possible exception to the above argument is that gyromotion couples the dust to the magnetic field in the perpendicular direction, but not in the parallel direction. To take an extreme case, slow waves in a low-β plasma (which have displacements mostly along the field) with $\lambda\!\!\!^{-}$ less than Equation (37) might primarily displace the gas, while the dust fails to participate. If the small-scale field is itself turbulent, however, grains may undergo changes in pitch angle and be forced to move with the gas (Lazarian et al. 2004).

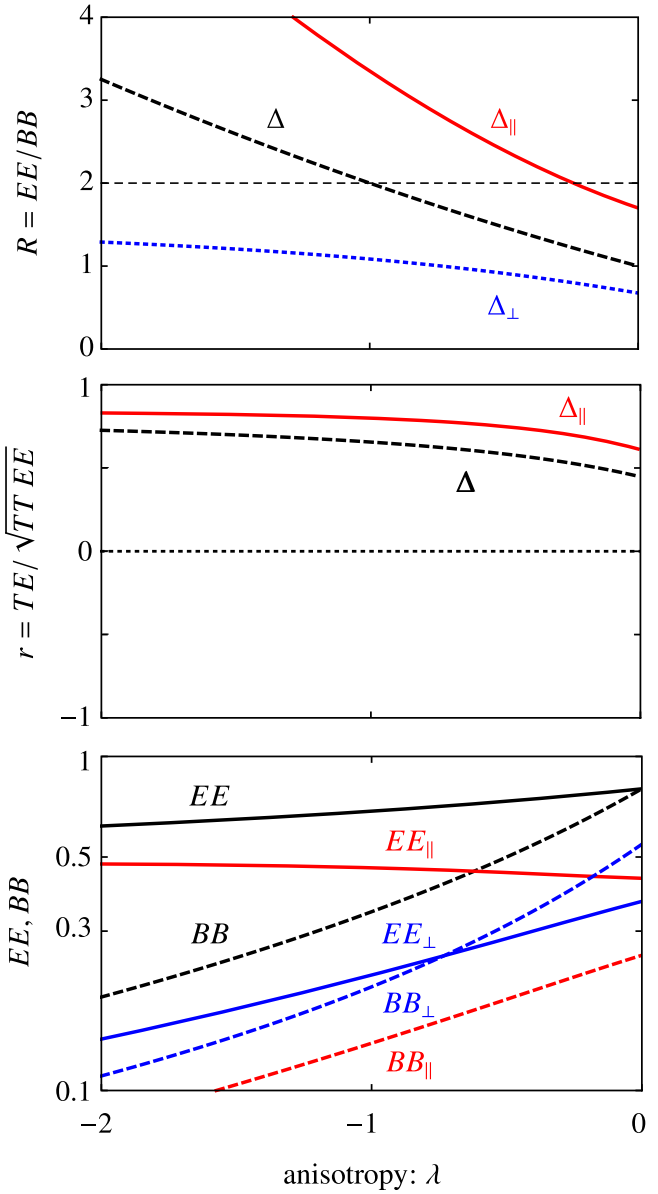

Figure 4. The *EE/BB* ratio (top), *TE* cross-correlation coefficient (middle), and *E*- and *B*-mode powers normalized to the displacement power spectrum (bottom) are shown for the model of fluid displacements (black), as well as the individual contributions by the longitudinal (red) and transverse (blue) displacements of the MHD fluid.

From an empirical perspective, the similarity of the power laws for the dust-intensity and dust-polarization power spectra; the difference between the *E*-mode and *B*-mode powers (Adam et al. 2016a, 2016b; Ade et al. 2016); the evidence for a similar *EE/BB* ratio in synchrotron radiation (Page et al. 2007); and the striking agreement of H I 21 cm and far-infrared dust maps (Schlegel et al. 1998) all suggest that the dust and plasma density are not grotesquely mismatched. If there is indeed some random component δn, not correlated with the magnetic field perturbation, then that should drive *EE/BB* toward unity, given the equality of the angular averages of the $\cos 2\psi$ and $\sin 2\psi$ factors that multiply δn in Equations (26) and (27). The observations thus suggest some correlation of the dust with the magnetic field. Moreover, when considering the results below, we should be looking not only for parameter combinations that provide $EE/BB \simeq 2$, but perhaps also for those that provide a larger ratio.

We thus proceed here under the assumption that the dust density traces the plasma density, but note that the validity of this assumption—and the consequences of its violation—warrant further investigation. Possibilities for testing the hypothesis include the frequency dependence of the dust-polarization signal (since dust segregation may depend on the grain size), cross-correlation with synchrotron polarization (which is emitted by the plasma, rather than the dust), and cross-correlation with polarized-starlight surveys.

8. Model of Random Displacements of the Magnetized Fluid

In the previous section we questioned whether the Planck dust-polarization data could be explained in terms of MHD turbulence and speculated that they might have more to do with the large-scale turbulence-driving physics. Here we propose a simple phenomenological model of fluctuations of the ISM that, as we will see, can easily produce the observed *EE/BB* ratio and *TE* correlation.

Instead of decomposing perturbations into slow/fast/Alfvén MHD waves, we here simply suppose that the magnetized fluid experiences a random displacement,

$$\boldsymbol{\Delta}(\boldsymbol{x}) = (\Delta_1, \Delta_2, \Delta_3). \tag{39}$$

The continuity equation then provides the associated density perturbation,

$$\frac{\delta n}{n_0} = -i\boldsymbol{k}\cdot\boldsymbol{\Delta} = -ik\,(\Delta_1\cos\psi + \Delta_2\sin\psi), \tag{40}$$

and from the MHD equation, $\delta\boldsymbol{H} = i\boldsymbol{k}\times(\boldsymbol{\Delta}\times\boldsymbol{H}_0)$, the associated magnetic field perturbations are,

$$\frac{\delta H_x}{H_0} = -\tan\psi\frac{\delta H_y}{H_0} = -ik\Delta_2\sin\theta\sin\psi \tag{41}$$

$$\frac{\delta H}{H_0} = ik\,(\Delta_3\sin\theta\cos\theta\cos\psi - \Delta_1\cos^2\theta\cos\psi - \Delta_2\sin\psi). \tag{42}$$

These are then inserted into Equations (23)–(24) to determine the *E*- and *B*-mode polarizations. To calculate the power, we assume the displacement field has equal power in all three components, $\langle\Delta_i\Delta_j\rangle = \delta_{ij}F_\lambda$, where λ now represents the anisotropy in the displacement power.

The results for the *EE/BB* ratio, *TE* cross-correlation coefficient, and individual powers are shown in Figure 4. This model easily explains the $EE/BB = 2$ ratio and positive *TE* correlation with a moderately anisotropic power index of $\lambda \simeq -1$.

To gain better insight into the physical mechanisms that could generate a spectrum of displacements, we decompose $\boldsymbol{\Delta}$ in the basis spanned by $\hat{\boldsymbol{k}}$, $\hat{\boldsymbol{a}}$, and $\hat{\boldsymbol{\theta}}$. We define longitudinal displacements as $\boldsymbol{\Delta}_\parallel = (\boldsymbol{\Delta}\cdot\hat{\boldsymbol{k}})\hat{\boldsymbol{k}}$ and transverse displacements $\boldsymbol{\Delta}_a$ and $\boldsymbol{\Delta}_\theta$. We immediately notice that the density perturbation is entirely due to longitudinal displacements,

$$\frac{\delta n}{n_0}\Big|_\parallel = -ik\Delta_\parallel. \tag{43}$$

Hence, the observed, strong *TE* cross-correlation implies that the longitudinal modes play a significant role in the structure of the ISM on these scales. The magnetic field fluctuations are

$$\frac{\delta H_x}{H_0} = -\tan\psi \frac{\delta H_y}{H_0} = -ik\sin\psi(\Delta_\parallel \sin\alpha \sin\varpi + \cos\alpha(\Delta_a \cos\varpi - \Delta_\theta \sin\varpi)) \quad (44)$$

$$\frac{\delta H}{H_0} = -ik(\Delta_\parallel \sin^2\alpha - \Delta_\theta \sin\alpha\cos\alpha). \quad (45)$$

Using the above results, we can assess the relative contributions of longitudinal- and transverse-displacement power to the *E*- and *B*-mode powers. A similar procedure as above is carried out to evaluate the *EE/BB* ratio, shown in Figure 4. The power in transverse displacements, indicated in the figure as $\Delta_\perp$, consists of the sum of Δ_a and Δ_θ modes. In the context of this model, the observations suggest a slightly anisotropic spectrum of longitudinal displacements. Although there is some dependence of the *EE/BB* ratio on λ, the dependence is relatively weak.

In addition to being fairly simple, this random-displacement model is also fairly robust. There is variation in *EE/BB* and *TE* with the anisotropy parameter λ. However, the *TE* correlation is generically positive and the variation of *EE/BB* with λ is fairly slow. Clearly, this model falls far short of a theory. Still, it has strengths as a working model that may help guide a more robust astrophysical explanation for the observations.

9. Conclusions

We have demonstrated that the *EE*, *BB*, and *TE* power spectra for polarized dust (and synchrotron) emission provide a new, unique, and powerful probe of the state of the magnetized ISM. Using a toy model of the ISM to illustrate the application of these new tools, we calculated the contributions to *E*- and *B*-mode powers and the *TE* cross-correlation from the slow, fast, and Alfvén waves MHD waves and and provided results for different ratios β of magnetic field to gas pressures and different power anisotropies. We argued that the observations —of *EE/BB/TE* power and the spectral index for fluctuations— greatly reduce the available parameter space of MHD turbulence models for the *Planck* dust-polarization data. We then speculated that a full explanation of the observations may involve the effects of the large-scale physics and developed a simple phenomenological model, based on random displacements of a magnetized fluid, that can account for the observations.

This toy model is limited in several important ways. It assumes a single-component ISM, in which dust traces the plasma. The model also does not explicitly account for the filamentary structure of the ISM. Future work will have to address these issues. It may turn out that a more realistic model that accounts for multicomponents and anisotropic structures will populate the basis of MHD waves in such a way to explain the *EE/BB* ratio.

Our work motivates a vast suite of additional investigations. First of all, we have used here only the fact that the *TE* cross-correlation coefficient is positive. *Planck* has published results for *TE* power, and for the *TT* and *EE* powers, but those are separate analyses that use different cuts and assumptions about systematic effects. It will be valuable to measure more carefully the cross-correlation coefficient we have calculated here. Second, we have presented results for *EE/BB* ratios and the *TE* cross-correlation after averaging over all magnetic field orientations because the observed $EE/BB \simeq 2$ ratio seems to be quite generic across the sky. Still, the background-field orientation may differ from one small patch of sky to another, so the *EE/BB* ratio and *TE* correlations should also vary. If the background field has a fixed orientation in some small patch of sky, then there should also be a local departure from statistical isotropy within that patch. There is also potentially interesting information in the ℓ dependence of the C_ℓ. Is it really a power law? Or does it steepen at higher ℓ? Are the ℓ dependences of the *EE*, *BB*, *TE*, and *TT* power spectra all the same? Or are there subtle variations that may reflect scale-dependent anisotropies or perhaps some other physics not accounted for here? We also suggest further investigation of the frequency dependence of dust-polarization maps and cross-correlation with synchrotron-polarization maps and starlight polarization surveys to test the hypothesis that the dust density traces the plasma density assumed here. Finally, although we have focused here on *Planck* dust-polarization maps, similar techniques can also be applied to dust-polarization data from specific molecular clouds.

Fortunately, there is not only far more along these lines that can be done with existing *Planck* data, but also prospects for rich new data sets to build upon *Planck*'s findings.

We thank E. Vishniac for useful discussions. M.K. was supported by NSF Grant No. 0244990, NASA NNX15AB18G, the John Templeton Foundation, and the Simons Foundation. R.R.C. was supported by DOE grant DE-SC0010386. C.H. was supported by NASA, the U.S. Department of Energy, the David & Lucile Packard Foundation, and the Simons Foundation.

References

Adam, R., Ade, P. A. R., Aghanim, N., et al. (Planck Collaboration) 2016a, A&A, 586, A133
Adam, R., Ade, P. A. R., Aghanim, N., et al. (Planck Collaboration) 2016b, A&A, 586, A135
Ade, P. A. R., Aghanim, N., Alina, D., et al. (Planck Collaboration) 2015a, A&A, 576, A104
Ade, P. A. R., Aghanim, N., Alina, D., et al. (Planck Collaboration) 2015b, A&A, 576, A105
Ade, P. A. R., Alves, M. I. R., Aniano, G., et al. (Planck Collaboration) 2015c, A&A, 576, A107
Ade, P. A. R., Aghanim, N., Alves, M. I. R., et al. (Planck Collaboration) 2015d, A&A, 594, A25
Ade, P. A. R., Aghanim, N., Arnaud, M., et al. (Planck Collaboration) 2016, A&A, 586, A141
Aghanim, N., Alves, M. I. R., Arzoumanian, D., et al. (Planck Collaboration) 2016, A&A, 596, A105
Ali-Haimoud, Y., Hirata, C. M., & Dickinson, C. 2009, MNRAS, 395, 1055
Andersson, B.-G., Lazarian, A., & Vaillancourt, J. E. 2015, ARA&A, 53, 501
André, P., et al. 2010, A&A, 518, L102
Armstrong, J. W., Rickett, B. J., & Spangler, S. R. 1995, ApJ, 443, 209
Brandenburg, A., & Lazarian, A. 2013, SSRv, 178, 163
Cabella, P., & Kamionkowski, M. 2004, arXiv:astro-ph/0403392
Chandrasekhar, S., & Fermi, E. 1953, ApJ, 118, 113
Cho, J., & Lazarian, A. 2002, PhRvL, 88, 245001
Cho, J., Lazarian, A., & Vishniac, E. 2003, LNP, 614, 56
Clark, S. E., Hill, J. C., Peek, J. E. G., Putman, M. E., & Babler, B. L. 2015, PhRvL, 115, 241302
Clark, S. E., Peek, J. E. G., & Putman, M. E. 2014, ApJ, 789, 82
Delabrouille, J., Betoule, M., Melin, J.-B., et al. 2013, A&A, 553, A96
Dolginov, A. Z. 1972, Ap&SS, 18, 337
Dolginov, A. Z., & Mytrophanov, I. G. 1976, Ap&SS, 43, 257
Draine, B. T. 1985, in Protostars and Planets II, ed. D. C. Black & M. S. Matthews (Tucson, AZ: Univ. Arizona Press), 621

Draine, B. T., & Fraisse, A. A. 2009, ApJ, 696, 1 [Erratum: ApJ 757, 106(2012)]
Draine, B. T., & Lazarian, A. 1998, ApJL, 494, L19
Draine, B. T., & Weingartner, J. C. 1996, ApJ, 470, 551
Draine, B. T., & Weingartner, J. C. 1997, ApJ, 480, 633
Dunkley, J., Amblard, A., Baccigalupi, C., et al. 2009, in AIP Conf. Proc. 1141, CMB Polarization Workshop: Theory and Foregrounds: CMBPol Mission Concept Study, ed. S. Dodelson et al. (Melville, NY: AIP), 222
Elmegreen, B. G., & Scalo, J. 2004, ARA&A, 42, 211
Essinger-Hileman, T., Ali, A., Amiri, A., et al. 2014, Proc. SPIE, 9153, 91531I
Finkbeiner, D. P., Langston, G. I., & Minter, A. H. 2004, ApJ, 617, 350
Fissel, L. M., Ade, P. A. R., Angile, F. E., et al. 2010, Proc. SPIE, 7741, 77410E
Fosalba, P., Lazarian, A., Prunet, S., & Tauber, J. A. 2002, ApJ, 564, 762
Goldreich, P., & Sridhar, S. 1995, ApJ, 438, 763
Goodman, A. A., Bastien, P., Menard, F., & Myers, P. C. 1990, ApJ, 359, 363
Haverkorn, M., Brown, J. C., Gaensler, B. M., & McClure-Griffiths, N. M. 2008, ApJ, 680, 362
Heiles, C. 1996, ApJ, 462, 316
Heiles, C., & Troland, T. H. 2003, ApJ, 586, 1067
Hennebelle, P. 2013, A&A, 556, A153
Inoue, T., & Inutsuka, S. 2016, arXiv:1608.02601
Iroshnikov, P. S. 1964, SvA, 7, 566
Kalberla, P. M. W., & Kerp, J. 2016, A&A, 595, 37
Kamionkowski, M., Kosowsky, A., & Stebbins, A. 1997a, PhRvL, 78, 2058
Kamionkowski, M., Kosowsky, A., & Stebbins, A. 1997b, PhRvD, 55, 7368
Kamionkowski, M., & Kovetz, E. D. 2014, PhRvL, 113, 191303
Kamionkowski, M., & Kovetz, E. D. 2016, ARA&A, 54, 227
Kataoka, A., Machida, M. N., & Tomisaka, K. 2012, ApJ, 761, 40
Kim, C.-G., Kim, W.-T., & Ostriker, E. C. 2006, ApJL, 649, L13
Koch, P. M., Tang, Y.-W., & Ho, P. T. P. 2013, ApJ, 775, 77
Kovetz, E. D., & Kamionkowski, M. 2015, PhRvD, 91, 081303
Kraichnan, R. H. 1965, PhFl, 8, 1385
Kritsuk, A. G., & Norman, M. L. 2002, ApJL, 569, L127
Lacki, B. C. 2013, arXiv:1308.5232
Lazarian, A., & Yan, H. 2002, ApJL, 566, L105
Lazarian, A., Yan, H., & Draine, B. T. 2004, ApJ, 616, 895
Lithwick, Y., & Goldreich, P. 2001, ApJ, 562, 279
Matsumura, T., Akiba, Y., Borrill, J., et al. 2013, JLTP, 176, 733
Misawa, R., Bernard, J-Ph., Ade, P., et al. 2014, Proc. SPIE, 9153, 91531H
Miville-Deschenes, M.-A., et al. 2010, A&A, 518, L104
Molinari, S., et al. 2010, A&A, 518, L100
Niemack, M. D., Ade, P., de Bernardis, F., et al. 2015, arXiv:1509.05392
Norman, C. A., & Ferrara, A. 1996, ApJ, 467, 280
O'Dea, D. T., Clark, C. N., Contaldi, C. R., & MacTavish, C. J. 2012, MNRAS, 419, 1795
Padoan, P., Pan, L., Haugbølle, T., & Nordlund, Å. 2016, ApJ, 822, 11
Page, L., Hinshaw, G., Komatsu, E., et al. 2007, ApJS, 170, 335
Pelkonen, V.-M., Juvela, M., & Padoan, P. 2007, A&A, 461, 551
Rybicki, G. B., & Lightman, A. P. 1979, Radiative Processes in Astrophysics (New York: Wiley)
Schekochihin, A. A., Cowley, S. C., Dorland, W., et al. 2009, ApJS, 182, 310
Schlegel, D. J., Finkbeiner, D. P., & Davis, M. 1998, ApJ, 500, 525
Seljak, U. 1997, ApJ, 482, 6
Seljak, U., & Zaldarriaga, M. 1997, PhRvL, 78, 2054
Shebalin, J. V., Matthaeus, W. H., & Montgomery, D. 1983, JPlPh, 29, 525
Soler, J. D., Hennebelle, P., Martin, P. G., et al. 2013, ApJ, 774, 128
Stein, W. 1966, ApJ, 144, 318
Voelk, H. J., Jones, F. C., Morfill, G. E., & Roeser, S. 1980, A&A, 85, 316
Zaldarriaga, M. 2001, PhRvD, 64, 103001
Zaldarriaga, M., & Seljak, U. 1997, PhRvD, 55, 1830